THE AMERICAN SOCIETY OF MECHANICAL ENGINEERS
345 E. 47th St., New York, N.Y. 10017

95-GT-325

NUMERICAL ANALYSIS OF INTRA-CAVITY AND POWER-STREAM FLOW INTERACTION IN MULTIPLE GAS-TURBINE DISK-CAVITIES

by
M.M. Athavale and A.J. Przekwas
CFD Research Corporation
Huntsville, AL
and
R.C. Hendricks and B.M. Steinetz
NASA Lewis Research Center
Cleveland, OH

ABSTRACT

A numerical analysis methodology and solutions of the interaction between the power stream and multiply-connected multi-cavity sealed secondary flow fields are presented. Flow solutions for a multi-cavity experimental rig were computed and compared with experimental data of Daniels and Johnson. The flow solutions illustrate the complex coupling between the main-path and the cavity flows as well as outline the flow thread that exists throughout the subplatform multiple cavities and seals. The analysis also shows that the de-coupled solutions on single cavities is inadequate. The present results show trends similar to the T-700 engine data that suggests the changes in the CDP seal altered the flow fields throughout the engine and affected the engine performance.

INTRODUCTION

As power systems mature the ability to refine component efficiencies declines. Current efforts in the gas turbine industry are centered on the interactive flow systems such as the interaction between the power stream and the secondary flow paths existing beneath the blade platforms, beyond the blade/vane tips and around the diffuser and combustor sections (Athavale, et al, 1994(a); Chew et al. 1994; Green and Turner 1994; Hah, 1984, 1992; Hendricks et al. 1994(a)). In most cases the secondary flows provide the necessary component cooling, for example, compressor gas flowing about the combustor liner and through the turbine stators.

In the conventional turbomachine design, component analyses are often carried out independently with the power stream flow data taken as a passive boundary condition. And for large changes in component efficiencies this approach has been more than adequate. However, as gains in component efficiencies diminish, the interaction becomes acute. Recent experimental evidence illustrates this point. Changing the compressor discharge seal (CDP) from a 6 forward facing tooth labyrinth to a two stage brush seal provided at least a 1 percent decrease in specific fuel consumption (SFC). But more importantly, the compressor discharge pressure increased signaling a complete change in the compressor, combustor, and turbine pressure maps; in short changing the CDP seal changed in interaction between the secondary and power streams (Hendricks, et al., 1994 (b)).

Agreement between experimental evidence and numerical results for single cavities can provide good first order estimates of mass, heat, and momentum distributions. (Hendricks, et al., 1994 (a), Chew, others) For multiple cavity experiments such as UTRC simulation of the space shuttle main engine high pressure fuel turbopump (SSME/HPFTP) (Daniels and Johnson 1993) the interactive effects of the power stream and secondary flow streams are simulated. Intercavity feedback affect pressure balancing and stator/blade stage pressures throughout the entire turbomachine.

The current state-of-the-art Computational Fluid Dynamics (CFD) methodologies and tools are mature to a point where the analysis of multiple cavities with multiple interconnections and interaction with the main-path flows can be conducted. Herein, a numerical simulation of the UTRC HPFTP experimental scaled model rig provides mass distribution comparisons with experiment and flow

Presented at the International Gas Turbine and Aeroengine Congress and Exposition
Houston, Texas - June 5-8, 1995

streamlines to augment understanding of these measurements. These simulations prove the capabilities of the CFD tools to analyze the complex flow fields in complex flow geometries to provide accurate results. Such simulations provide details of the flow fields in engines and rigs that can be valuable in optimization of engine seals and cavity design as well as aid in design of experimental rigs for optimum instrumentation. While much work remains, the computed distribution of ingested mass and purge/coolant mass streams illustrates the importance of secondary/power stream interactions.

GEOMETRIC AND TEST PARAMETERS

The experimental apparatus simulating the SSME HPFTP is described by Daniels and Johnson (1993); however some critical details such as interstage seal and subplatform flow areas required information from the monitors (e.g. Elizabeth Messer, NASA MSFC Alabama) or the manufacturer (Rockwell/Rocketdyne Division). Figure 1a illustrates the UTRC simulation of the turbomachine, Figure 1b the model seal and gas source and measurement locations UTRC simulation, and Figure 1c the numerical block gridding as scaled and scanned directly from the drawings shown in the UTRC simulation (Daniels and Johnson (1993)).

Two-dimensional, axisymmetric analysis was assumed although the cost of a three-dimensional analysis may be justified for new designs and for the more exact computations, CAD drawings or equivalent would be required. The experimental rig contained several details, which make the flow 3-dimensional, and approximations were made to facilitate the axisymmetric analysis. The bolt heads on the rotor disks were neglected. The stationary support for the central seal contained slots in the circumferential direction. These were simulated as an open passage at the mean radius (domain connecting regions II and III). The radial width of this slot was fixed to yield the correct opening area in the actual rig. The interstage labyrinth seal was modeled exactly with the correct tooth shape and seal clearance.

The experimental rig also contained curved passages under the blade platform to simulate a portion of the blades. These passages were represented using rotating openings under the blade platforms in the 2-D flow field. The rotation of these passages offers some resistance to the flow going across and this effect in the 2-D flow was simulated by adding additional flow resistance. Momentum sinks proportional to the local dynamic head were added to the x and r momentum equations of all cells in regions V and VI. Thus, e.g. a sink term of type $1/2k_u\rho u^2$ was added to the x/u momentum equation and $1/2k_v\rho v^2$ was added to the x/v momentum equation where u and v are cartesian velocities in the axial and radial directions and ρ is the fluid density. The values of k_u and k_v were unknown, and a range of values from 0 to 100 were tried to see their effect on the flow field. The effects tended to be fairly small due to the small velocities through these passages. A value of 30 was used in the computations.

Test runs 102, 202, and 205 UTRC report (Daniels and Johnson (1993)) were selected to illustrate the effects of changing the forward cavity purge flows and tangential Reynolds number with air as the coolant, see Table 1.

FLOW GEOMETRY, CONDITIONS, AND SOLVER DESCRIPTION

The complex shapes of the cavities and passages precludes the use of a single block grid topology for computational simulations. In the present calculations, the overall flow domain was divided into 52 blocks (subdomains) to optimize the grid distribution, both in terms of the cell numbers and flow resolution. The flow domain included the four main powerstream or gas paths, four cavities, a labyrinth seal, open areas under the blade platforms, and the open area in the stator connection regions II and III (Figures 1b and 1c). A total of 18450 cells were used to discretize the flow domain. The computationally intensive nature of the runs precluded a detailed grid refinement analysis to ensure grid independence of the solutions. However, the grid was refined in the fish mouth seal areas and under the blade platform area to generate another grid with approximately 29,000 cells. Solutions on this grid were obtained for run #202. One of the important sets of parameters is the rates of flow ingress/egress at the rim seals (seals no. 1,2, 3, and 4) and these values for the coarse and fine grid were calculated and compared. These results are presented in Table 2 along with the results for other runs. It was observed that the flow rates through seals 2 and 4 remained nearly constant as the grid was changed, but the flow rates in seal numbers 1 and 3 changed through a larger extent (8-10%). In both cases, the flow rates through seals 1 and 3 reduced in absolute value. This will certainly have some effect on the concentration of the mass fraction F5 and in regions to the left of seal 3, but for the present purpose, the accuracy of the coarser grid was felt to be acceptable.

The flow simulations also included the energy equation, which needed boundary specification on all walls. In the absence of specific temperature and/or heat flux information, the walls were assumed to be adiabatic. Since the experiments were run at room temperatures with nearly the same temperatures for all flow streams, the net temperature changes in the flow field were small (~ 40°K) and were produced mainly as a result of windage. Under these conditions, the adiabatic wall assumption was justified. However, in an actual engine, the temperatures of the various main and passage flows are widely different, and assumption of adiabatic walls will incur a higher error in solutions in these cases. In the absence of wall information, the solid disks and supports should be included in the energy equation computations and the conditions at the wall should be computed as a part of the solution. The present CFD code is capable of handling this situation; such an analysis, however, will need additional grid blocks in all the pertinent solid regions to obtain a coupled fluid-solid energy equation solution.

The boundary conditions on main gas paths were:

measured, constant velocity values at the inlets, and measured static pressures at the exit boundaries. The purge velocities were calculated using the non-dimensional flow parameters and the measured density values (Daniels and Johnson (1993)). The velocity values were then used as inlet conditions at the respective purge flow locations. All rotor surfaces, including those in the open area under the blade platforms (connecting regions I and II, and III and IV) were specified as rotating walls.

Flow solutions were obtained using a multi-block version of SCISEAL (Athavale et al (1994 (b)), a pressure-based, finite volume, 3-D CFD code developed for flow and force calculations in turbomachinery seals. To simulate the tracer gas flows, different compositions of gases were specified at different inlet locations. The individual compositions were set very close to that of the air with minor changes in the CO_2 concentrations. The movement of these mixtures in the flow was tracked by solving mixture fraction equations for each of the individual compositions. The turbulent flow was solved using the standard k-ε turbulence model with wall functions. Second-order central-differencing was used for the convective fluxes with a damping of 20%, i.e. the convective fluxes were a combination of 20% upwind and 80% central differencing. As remarked upon earlier, a flow resistance was added to the momentum equations in regions V and VI to simulate blade shank resistance.

NUMERICAL RESULTS

One of the important parameters in these experiments was the flow movement across the four fish-mouth rim seals separating the power stream or main-gas-path and the cavities. Experimental observations show that in all three runs, seals No. 1 and 2 which are on either side of the rotor I, always ingest flow from the main gas path. This mass and the purge flow mass then exits through seals 3 and 4, on rotor II. Ingestion through rim seals 1 and 2 was designed intentionally, so that the temperatures in the blade shanks in rotor 1 are higher which reduces the thermal gradients in the blade platform and shank regions. The computed mass flow rates at all "inlets" on the overall flow domain are compared with the experimental values in Table 2. The net mass in (through seals 1 and 2, and all purge flows) and the net mass out (seals 3 and 4) are also shown. As seen from the table, very good agreement is seen in the mass ingestion rates on seals 1 and 2. The measured values of the flow egress in seals 3 and 4 are lower than the calculated values. An overall mass balance for experimental values indicates that the mass egress is substantially lower than mass input, and hence the actual mass flow values in seals 3 and 4 should be higher than those measured, for mass conservation.

To illustrate the flow structure and the flow thread within the cavities, the streamlines are plotted in Figures 2a and 2b for baseline run No. 202. Seal 1 ingests main path flow and this flow is forced on along the top wall of the blade shank region (Region V), due to the rotor disk rotation, and due to the purge flow in Region I that gets pumped up along the rotor surface. The combined flow of ingested gas and purge flow then passes through the blade shank regions into Region II, where the ingested flow in seal 2 mixes with it. The entrained powerstream flow near seal 2 goes through a complicated path to get into Region II. A vortex at the fish-mouth rim seal ingests flow (see Figure 2c) on its downstream side, which then goes through seal 2. This is entrained by another vortex on the other side of seal 2 and then eventually mixes with the flow from the blade shank passage.

This mixture then passes along the top wall of Region II, forced towards this wall by a recirculation bubble generated by pumped flow along the rotor wall in Region II. This flow then passes through the slots in the stator wall in Region III, and up along through seal 3, and the other half through the blade shank region in rotor 2, and eventually out through seal No. 4. This overall pattern is dictated by the "flow pumping" induced at rotor walls, and the pressure differentials at the four main-path regions. Variations in the purge flow rates (runs 202 and 205) and variation in the tangential Reynolds number (runs 102 and 205) essentially show the same main features of the flow field (see Table 1). The variation in the flow rates and rotating speed serves to change the strength of the vortical patterns and the streamlines.

On a region-by-region basis, we see that in region I and IV, most of the flow domains are filled with the purge flow mixtures F1 and F3, and these will provide efficient disk cooling. Near seal 1, and region V, the purge flow F1 mixes with ingested flow F4. Flows in region V and VI are dominated by a recirculation bubble generated by the wall rotation. In a 3-D flow one can expect that the flow structure will be different in these regions due to presence of blade shank walls.

Mixing of F1, F4 and F5 near the joining of regions II and V follows a tortuous route. The large recirculation bubble in region V interacts with a smaller bubble at this junction before the flow exits into region II, where this stream further mixes with purge flow F2. The flow pattern indicates that the cool purge flow rides along the rotor wall and mixes with the big stream at the top of region II. The presence of large amounts of F2 on rotor wall also indicates efficient cooling.

The mixture of F2, F4, F5 and F1 passes then to region III, where it mixes with a small amount of F2, coming through the labyrinth seal. In region III, the main flow thread hits the rotor wall much earlier than in regions I and II. The cooling of this wall can be expected to be poorer than rotor I walls. On the other side of the rotor, region IV, there is very little ingress of the mixture coming through region VI and the rotor wall cooling is more effective. This uneven cooling of rotor I could lead to thermal stresses in the disk and disk warpage.

The distribution of the ingested and purged flows can also be shown using the concentrations of the various gas compositions (F1 through F7) injected in the main and purge paths. Experimental data and computed results indicate that most of Region I is occupied by purge flow F1, and region IV is occupied by purge F3. Most of the mixing and ingestion takes place in regions II, III and areas near the rim seals.

Figure 3a through 3f show contours of concentration values for various compositions used in the main path and purge flows: (1) purge flow F1 in region I (Figure 3a); (2) purge flow F2 injected in the center of the rig (Figure 3b); (3) main path flow F4 at seal 1 (Figures 3c and 3d); and (4) main path flow F5 at seal 2 (Figure 3e and 3f). The computations as well as experiments show no evidence of concentrations of F6 (seal 3) and F7 (seal 4) which indicate no ingestion through these seals. The contours of F2 (Figure 3b) indicate the pumping action of rotor I and II that splits F2 flow to the right in cavity II and to left in cavity III through the labyrinth seal. The placement and values of these contours are consistent with the flow structure seen in Figures 2a and 2b. The purge flow F1 and the ingested flow F4 (Figures 3a, 3c, and 3d) also mix in regions II and III as seen from contours for F1 and F4 (Figures 2c and 2d). The blade shank region in rotor 2 then passes some of this mixture in Region IV and out through seal 4. The contours for these concentrations for runs 205 and 102 (not shown herein) also show similar structures, consistent with the flow behavior in these runs.

The calculated values of the concentrations of the various gas compositions were obtained at several probe locations, and compared with the experimental values. Some representative concentration values of the various compositions in Regions I through V are shown in Table 3, along with the experimentally measured values. The locations of the probes are shown in Table 3. The computed values in and around region II and III show good correlation with experiments. However, the match deteriorates in and around the blade shank regions, and some of the fish mouth rim seals. The 2-D treatment of the blade shanks is partly responsible for the discrepancy. The discrepancy at fish mouth rim seals could be in part due to the inaccuracies in the shapes of the seal outlines, introduced during scanning of the drawings in the UTRC report (Daniels and Johnson (1993)) which were used to generate grids. The computational effort to simulate the blade shank passages in 3-D would require upwards of 0.3M to 0.5M points and several weeks to computational time to complete; for this analysis such an effort was not required.

In general the streamlines show a secondary flow thread beneath the blade platform that essentially starts at the forward cavity, ingested fluid from seals 1 and 2, continues through the interstage area mixing with the purge flow to exhaust through seals 3 and 4, with flow additions from the aft cavity purge F3.

For the simulated geometric configuration, Figure 1, the major purge and coolant loop tends to favor the second stage turbine while encouraging fluid ingestion and mixing between the blade platforms and roots of the first stage turbine.

As a numerical exercise, it was found that nearly ten-fold increases in the purge flows F1 and F2 were required to inhibit the ingestion through seals 1 and 2 for the main gas path conditions and cavity 4 purge flow of run 202.

SUMMARY OF RESULTS

1. Multiple cavity analyses capture interactive power/secondary flow stream effects that can not be realized for uncoupled single cavity treatments. These flow streams define the subplatform flow thread.
2. Good agreement between analysis and data was seen in the mass ingestion rates on seals 1 and 2, with flow egress in seals 3 and 4 lower than the calculated values.
3. Both analysis and data illustrate ingestion at the first stage turbine leading and trailing edge rim seals with fluid mixtures of ingested gases and purge gases exiting at both the leading and trailing edge seals of the second stage turbine.
4. Comparisons of calculated results and data on concentrations of various flow compositions in the central cavity between the first and second stage rotors is good but deteriorates at the blade shank regions, and some of the fish mouth rim seals. The 2-D treatment and drawing scans may be partly responsible for the discrepancies.
5. For the given turbomachine geometry, the coolant and purge gas flows form a secondary flow thread that favors cooling of the second stage turbine disk, probably enhancing the thermal gradients in the first stage turbine disk.
6. Multiple cavities affect the flows throughout the engine; small changes in purge flows due to seal changes alters the engine flow fields. Experimental results of T-700 testing illustrate this effect.

REFERENCES

Athavale, M.M., Przekwas, A.J., Hendricks, R.C., and Steinetz, B.M. (1994 (a)) Comparison of Numerical Results and Multicavity Purge and Rim Seal Data with Extensions to Dynamics. Aerospace Today, June 1994.

Athavale, M.M., Przekwas, A.J., Hendricks, R.C., and Liang A. (1994 (b)) SCISEAL - A Three-Dimensional CFD Code for Accurate Analyses of Fluid Flow and Forces in Seals, Advanced ETO Propulsion Technology, NASA MSFC, Alabama, May 1994.

Chew, J.W., Green, T., Turner, A.B., 1994, Rim Sealing of Rotor-Stator Wheelspaces in the Presence of External Flow, Paper 94-GT-126, 39th ASME Int'l Gas Turbine and Aeroengine Conference Netherlands, June 13-16, 1994.

Daniels, W.A. and Johnson, B.V., 1993. Experimental Investigation of Turbine Disk Cavity Aerodynamics and Heat Transfer, Contract NAS8-37462, UTRC Report 93-957878-27.

Green, T., and Turner, A.B., 1994, J. Turbomachinery, April 1994, V. 116/327.

Hah, C., (1984), "A Navier-Stokes Analysis of Three-Dimensional Turbulent Flows Inside Turbine Blade Rows at Design and Off-Design Conditions," ASME J. Eng. in Gas Turbines and Power, vol. 106, pp. 421.429.

Hah, C., (1992), "Navier-Stokes Verification of Advanced Gas Generator Oxidizer Turbine Stage," NASA CP-3174, vol. 1, pp. 362-370.

Hendricks, R.C., Steinetz, B.M., Athavale, A.A., Przekwas, A.J., Braun, et al. (1994 (a)) Interactive Developments of Seals, Bearings, and Secondary Flow

Systems with the Power Stream. ISROMAC-5, May 1994, Hawaii,

Hendricks, R.C., Griffin, T.A., Kline, T.R., Csavina, K.R. Pancholi, A., Sood, D. (1994 (b)) Relative Performance Comparison Between Baseline Labyrinth and Dual-Brush Compressor Discharge Seals in a T-700 Engine Test. For presentation at 39th ASME International Gas Turbine and Aeroengine Conference,Netherlands, June 13-16, 1994.

Table 1. Test Parameters and Notation

Test No.	rpm	Pressure psia	Reynolds Number	Forward Cavity purge F1=ϕ_{12}	Center Cavity purge F2=ϕ_{13}	Aft Cavity purge F3=ϕ_{14}
102	1004	60.55	1.64E6	.027	.012	.012
202	1502	57.24	2.19E6	.017	.008	.013
205	1504	57.79	2.24E6	.030	.015	.014

Powerstream flow concentrations Nomenclature		Herein	UTRC	Seal No.
First stage blade	leading edge	F4 = ϕ_{01}		1
	trailing edge	F5 = ϕ_{03}		2
Second stage blade	leading edge	F6 = ϕ_{05}		3
	trailing edge	F7 = ϕ_{07}		4

Table 2. Experimental and Calculated Mass Flow Rates and Mass Balances

(Mass Flow rates in lbm/s)

Run No.	Rim Seal Flows				Specified Purge Flows				
	Seal 1	Seal 2	Seal 3	Seal 4	Forward Cavity	Center Cavity	Aft Cavity	Net, in $\dot{m}$	Net, out $\dot{m}$
102									
numerical	-0.150	-0.072	0.233	0.260	0.1425	0.0637	0.064	0.4923	0.4928
experimental	-0.126	-0.094	0.265	0.208	0.143	0.062	0.066	0.491	0.473
(exp-num)/exp	.19	-.23	.12	-.25	0	-.03	.03	.003	-.04
202									
numerical (18K grid)	-0.236	-0.139	0.286	0.353	0.1168	0.0552	0.0904	0.6374	0.639
numerical (30K grid)	-0.237	-0.126	0.283	0.33	0.1168	0.0552	0.0904	0.6374	0.639
experimental	-0.224	-0.154	0.257	0.271	0.115	0.057	0.087	0.637	0.528
(exp-num)/exp	.05	-.10	-.11	-.30	-.02	.03	.04	0	-.21
205									
numerical	-0.223	-0.1025	0.357	0.381	0.208	0.103	0.0985	0.7351	0.738
experimental	-0.186	-0.113	0.302	0.302	0.208	0.105	0.095	0.707	0.604
(exp-num)/exp	.20	.09	.18	.26	0	.01	.04	.04	.22

Net $\dot{m}_{in}$ = seal 1 + seal 2 + all purge flows

Net $\dot{m}_{out}$ = seal 3 + seal 4

$\Delta\dot{m} = (\dot{m}_{in} - \dot{m}_{out})$

$\Delta\dot{m} > 0$ implies net mass accumulation in apparatus

Run No.	$\Delta\dot{m}$ 102	202	205
experimental	+ 0.018	+ 0.109	+ 0.103
numerical	- 0.005	- 0.0006	- 0.0029

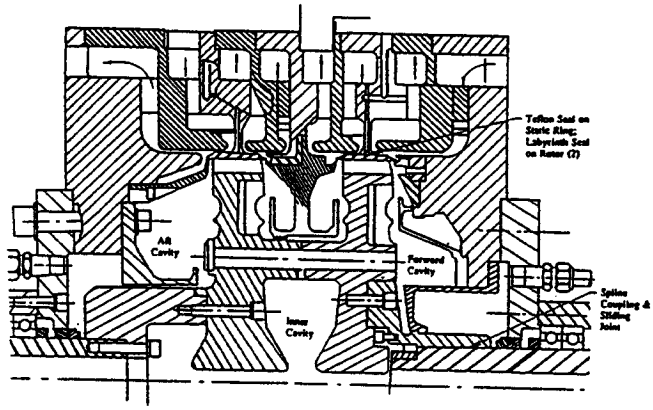

Figure 1a. Large-Scale Model of SSME HPFTP Disks and Cavities - From Daniels and Johnson (1993)

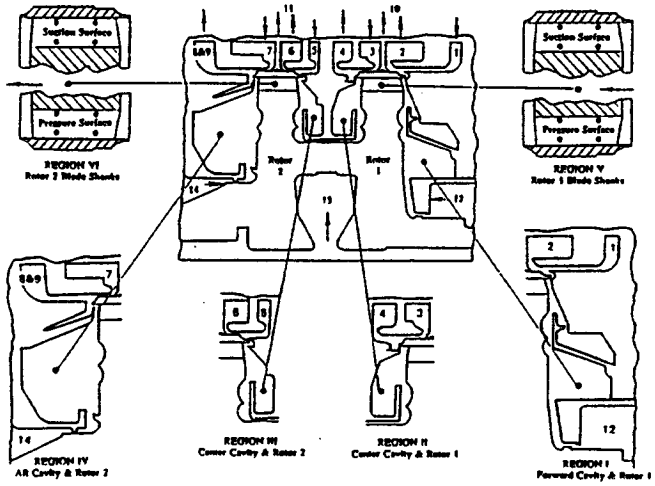

Figure 1b. Model Seal Region and Gas Source/Exit Locations - From Daniels and Johnson (1993)

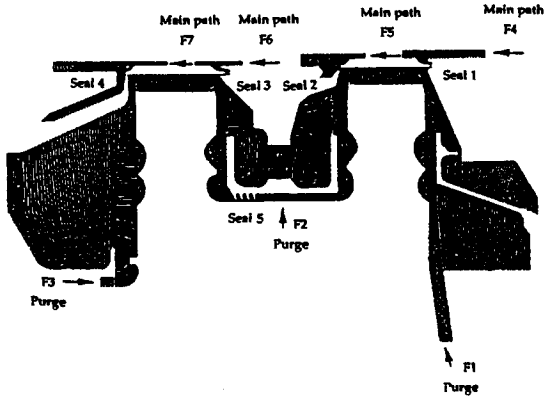

Figure 1c. Flow Domain Showing the Computational Grid and the Definition of Various Flow Streams and Rim Seal Locations

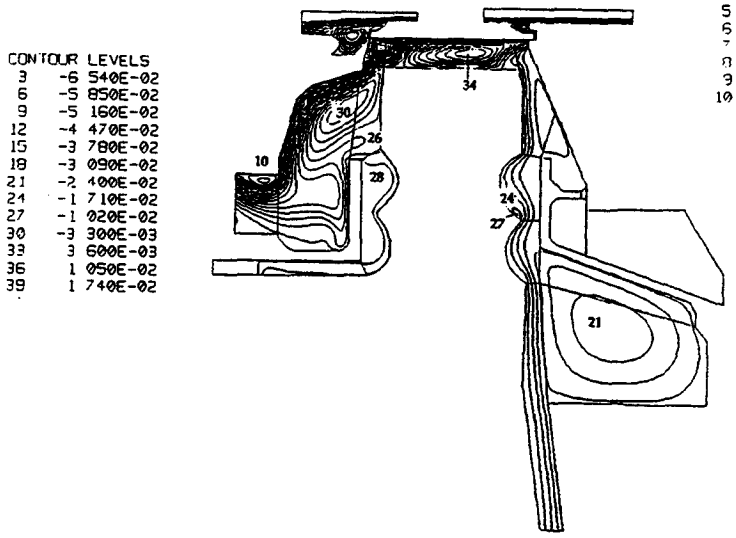

Figure 2a. Streamline Pattern in Regions I, II and the Connecting Blade Shank Region

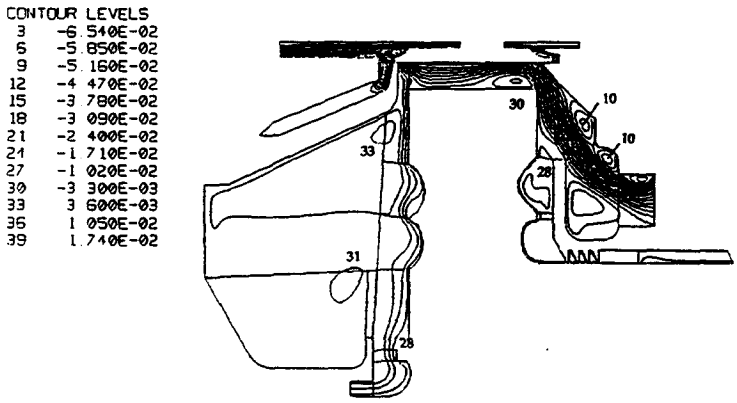

Figure 2b. Streamline Pattern in Regions III, IV, Connecting Blade Shank Region and the Slot in the Stator Support

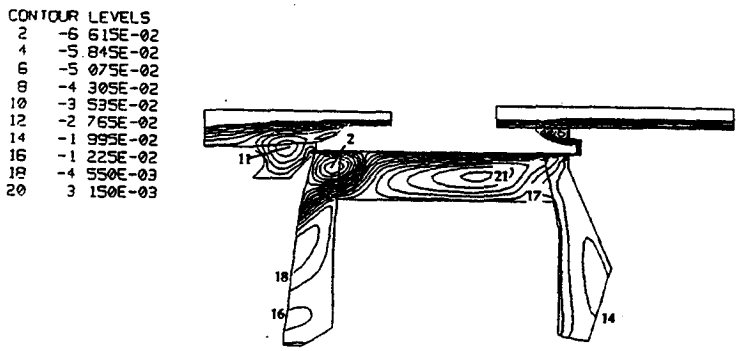

Figure 2c. Flow Detail at Seals 1, 2, and Blade Shank Region to Illustrate the Complex Vertical Structure and Main-Path Flow Ingestion

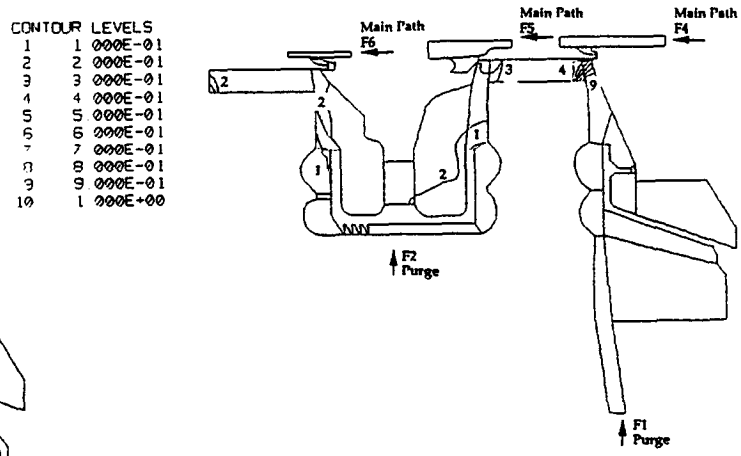

Figure 3a. Mass Fraction Contours of Purge Flow F1 in Regions I, II, and III, and the Blade Shanks (contour legends are the same for Figures 3a-3f)

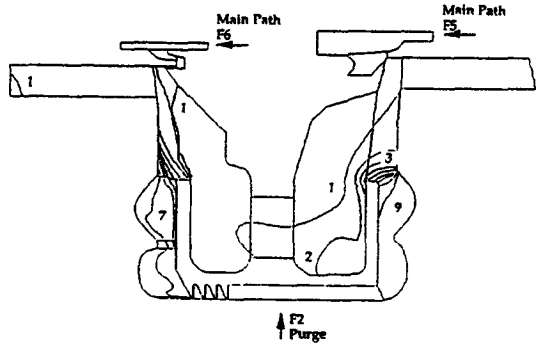

Figure 3b. Mass Fraction Contours of Purge Flows F2 in the Central Regions II and III, the Labyrinth Seal and Blade Shank

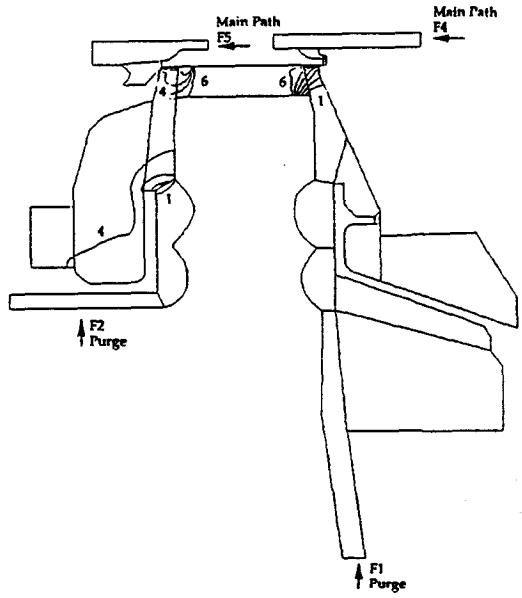

Figure 3c. Mass Fraction Contours of Ingested Powerstream Flow F4 in Regions I and II and Connecting Blade Shanks

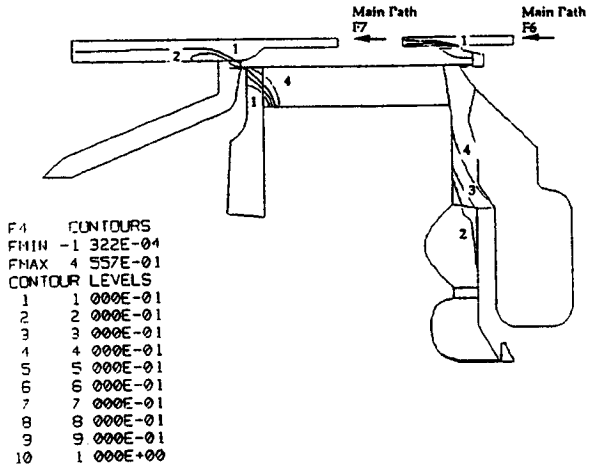

Figure 3d. Mass Fraction Contours of Ingested Powerstream Flow F4 in Regions III, IV, and Connecting Blade Shanks

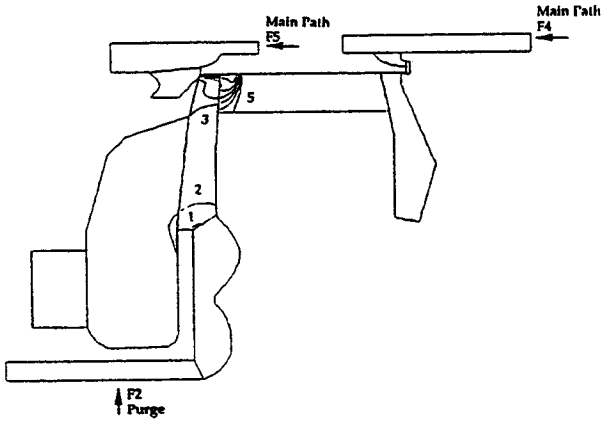

Figure 3e. Mass Fraction Contours of Ingested Powerstream Flow F5 in Regions I and II and Connecting Blade Shanks

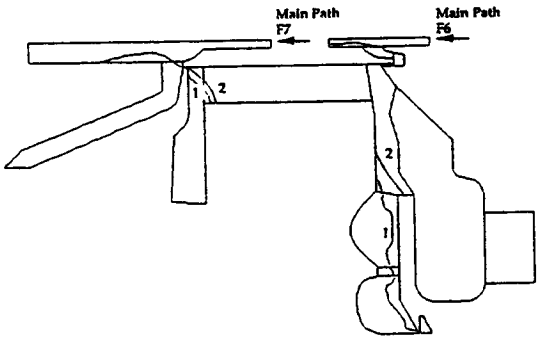

Figure 3f. Mass Fraction Contours of Ingested Powerstream Flow F5 in Regions III, IV, and Connecting Blade Shanks

Table 3. Comparison of Gas Source Measurements and Calculations for Flow Conditions Baseline Run 202 (see Table 1). See Figure 4 for Probe Locations.

	a_{12} F1	a_{13} F2	a_{14} F3	a_{01} F4	a_{05} F5
Region I - Forward Cavity					
A23 - numerical experimental	0.278 0.09	48-5 0	0 0	0.721 0.93	0.001 0
A24 - numerical experimental	0.978 0.96	1E-4 0	0 0	0.021 0.09	2E-4 0
Region II - Center Cavity and Rotor I					
C44 - numerical experimental	0.232 .24	0.03 .12	0 .03	0.465 .32	0.273 .28
C42 - numerical experimental	0.150 .22	0.378 .18	0 .03	0.299 .31	0.173 .22
A8 - numerical experimental	0.194 .09	0.194 .67	0 0	0.388 .13	0.223 .11
A5 - numerical experimental	0.003 .03	0.987 .9	0 0	0.006 .05	0.004 .04
C39 - numerical experimental	0.002 .07	0.992 .71	0 .03	0.004 .1	0.002 .04
Region III - Center Cavity and Rotor II					
B30 - numerical experimental	0.039 .06	0.838 .77	0 .03	0.078 .08	0.045 0
B26 - numerical experimental	0.070 .22	0.708 .22	0 .03	0.140 .29	0.082 .22
B23 - numerical experimental	0.216 .24	0.102 .12	0 .03	0.431 .33	0.251 .26
C25 - numerical experimental	0.218 .24	0.091 .11	0 .02	0.436 .33	0.254 .25
C33 - numerical experimental	0.097 .2	0.598 .19	0 .03	0.193 .31	0.112 .23
C29 - numerical experimental	0.223 .23	0.068 .11	0 .02	0.447 .33	0.261 .25
Region IV - Aft Cavity and Rotor II					
C31 - numerical experimental	0.006 .05	0.012 .03	0.956 .77	0.011 .07	0.007 .07
B10 - numerical experimental	0.213 .21	0.109 .12	0.004 .06	0.425 .34	0.248 .3

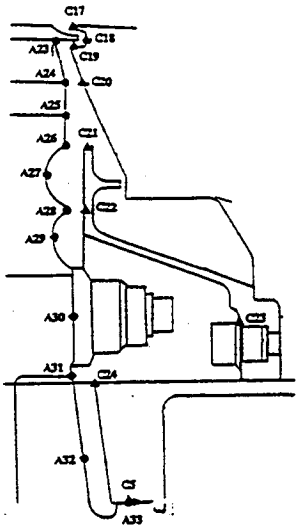

a. Region 1 and Rotor 1

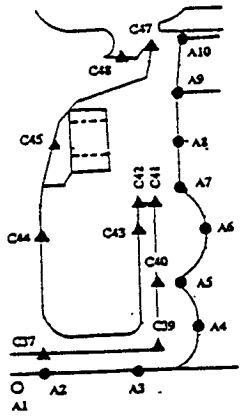

b. Region II and Rotor 1

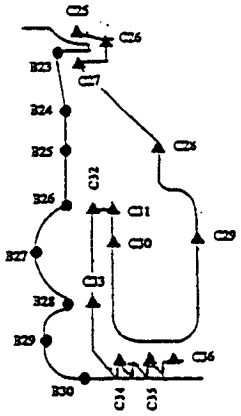

c. Region III and Rotor 2

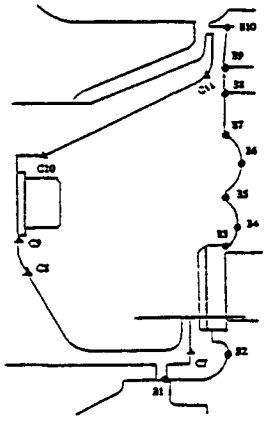

d. Region IV and Rotor 2

Figure 4. Locations of the Probes for Gas Source Measurements in Table 3. From Daniels and Johnson (1993)